The 2023 Mw7.8 Kahramanmaraş, Turkey Earthquake: An Overall-Subshear Rupture on Multi-segment Faults in Millennia Supercycle

Liuwei Xu[1], Saeed Mohanna[1], Lingsen Meng[1], Chen Ji[2], Jean-Paul Ampuero[3], Zhang Yunjun[4], Masooma Hasnain[1], Risheng Chu[5], Cunren Liang[6]

[1]Earth, Planetary and Space Sciences, UCLA. [2]Earth Science, UCSB. [3]Observatoire de la Côte d'Azur, Université Côte d'Azur. [4]Aerospace Information Research Institute, Chinese Academy of Sciences. [5]Innovation Academy for Precision Measurement Science and Technology, Chinese Academy of Sciences. [6]School of Earth and Space Sciences, Peking University.

Scan the QR code for our preprint on Research Square: Xu et al., 2023 (xuliuw1997@ucla.edu)

Summary

On February 6, 2023, an Mw7.8 earthquake hit the East Anatolian Fault (EAF) and Narlı Fault (NF), followed by an Mw7.5 event on the Sürgü Fault. We analyze multiple seismic datasets, GNSS recordings, and radar satellite images. Our study, using Slowness Enhanced Back-Projection and Finite Fault Inversion, reveals that the rupture originated on the NF, propagating 120 km northeast at 3.05 km/s and 200 km southwest at 3.11 km/s after reaching the EAF junction, exhibiting overall subshear speeds. Further analysis of Mach wave characteristics confirms the subshear rupture, matching the synthetic pattern predicted by close-Rayleigh speeds. The unexpectedly-large slip on some EAF segments suggests a supercycle lasting ≥900 years. The EAF geometry is similar to the San Andreas-San Jacinto Fault (SA-SJF) system, while the latter has higher slip rates. Given the absence of large earthquakes on SA-SJF's southern segments since 1857, an M8 earthquake could potentially occur there.

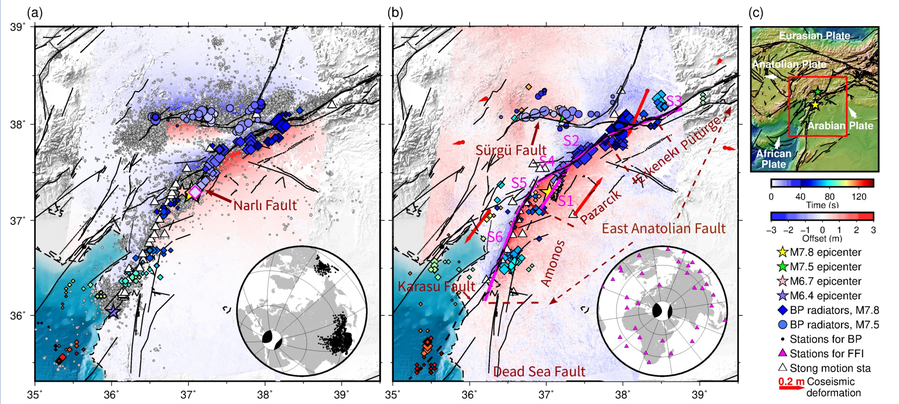

Figure 1. Spatiotemporal distribution of high-frequency (High-Freq) radiators and multiple datasets used in joint FFI. Diamonds denote the High-Freq radiators for the Mw 7.8 earthquake, color-coded by rupture time relative to the origin time of the event and with size proportional to the normalized BP power. Radiators imaged by the China array are shown in (a) and by the Alaska array are shown in (b). All China and Alaska stations are shown in the lower inset of (a). Color circles denote the same as diamonds but for the Mw 7.5 earthquake. Blue to red background shows the ground displacement in east-west direction (a) and in north-south direction (b) from radar satellites. (a) The gray dots denote the seismicities occurring from Jan 1st, 2023 to Mar 14th, 2023, from the AFAD catalog. (b) S1-S6 denote the vertical fault planes adopted for FFI. The red arrows indicate the coseismic deformation measured by GNSS stations. The white and magenta triangles denote the strong motion stations and teleseismic stations used by joint FFI, respectively. (c) The tectonic setting of the 2023 Mw 7.8 Kahramanmaraş earthquake.

Slowness Enhanced Back-Projection and Finite Fault Inversion

Slowness Enhanced Back-Projection (Meng et al., 2016): [dense and large-aperture China array, Alaska array (Figure 1a)] + [slowness calibrations derived using aftershocks along rupture path].

Joint Finite Fault Inversion (Ji et al., 2002):

local strong motion recordings, high-rate GNSS, teleseismic P and S waves, teleseismic Rayleigh and Love waves, InSAR and SAR images (Sentinel-1 range and azimuth offsets, ALOS InSAR and MAI, LuTan-1 InSAR).

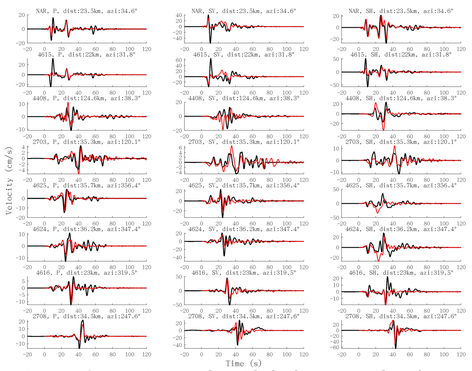

Figure 2. Strong motion recordings. Black: observation; red: synthetic.

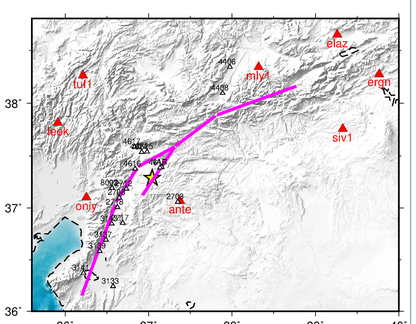

Figure 4. The station distribution. White: strong motion; red: GNSS.

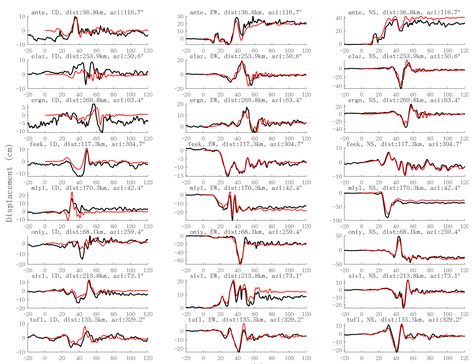

Figure 3. High-rate GNSS recordings.

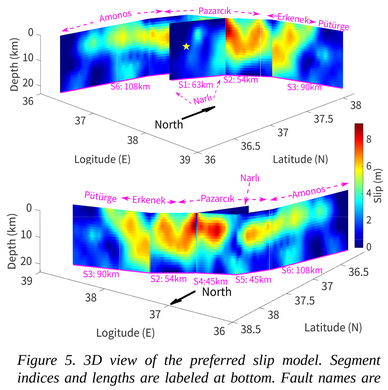

Figure 5. 3D view of the preferred slip model. Segment indices and lengths are labeled at bottom. Fault names are annotated on the top.

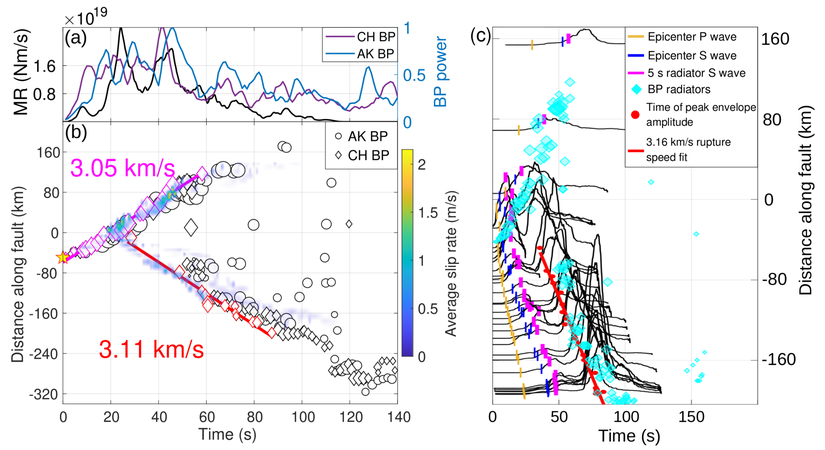

Figure 6. Spatial and temporal evolution of High-Freq radiators and slip rates. (a) The moment rate function (MR, black line) and the BP power for SEBP results of CH array (purple line) and AK array (blue line). (b) Along-fault distance and time of BP radiators and slip rates. The junction of the splay fault and the main fault is set as the origin of the distance axis, and the northeast is the positive direction. The origin time of the Mw 7.8 event is set as the origin of the time axis. The diamonds and circles denote the High-Freq radiators imaged by the CH and AK arrays, respectively. The colormap denotes the slip rate averaged across depth. The red and magenta slants show the fitted rupture speeds for the SW and NE fronts delineated by High-Freq radiators, respectively. (c) Vertically exaggerated envelopes of detrended, demeaned, bandpass filtered (1-4 Hz) fault-parallel components of strong motion stations shown in Figure 1a. The red line indicates the SW speed fit using the timing and distance of second envelope peaks at southern stations. The red dots indicate the time at which these peaks occur for a particular station's distance along the fault.

Mach Wave Searching and Analysis

Mach wave and Mach cone should be observed if rupture is long and has persistent supershear speed (Vallée & Dunham, 2012): (1) At a pair of azimuths around the rupture direction, surface waves waveform shapes are highly similar between the mainshock and a nearby EFG event (e.g., an M5-6 aftershock or foreshock). (2) The waveform amplitude ratio between the mainshock and the EGF event should equal their seismic moment ratio.

We find that the azimuthal distributions of CCs and amplitude ratios are distinct from those predicted by a supershear rupture. Here the CC and amplitude ratios peak at the two rupture directions rather than on their sides. This distribution pattern is consistent with simulation results of a subshear rupture traveling at Rayleigh wave speed ($V_{Rayleigh}$ = 0.92 Vs; Figures 7 & 8: observation, Figure 9: synthetic).

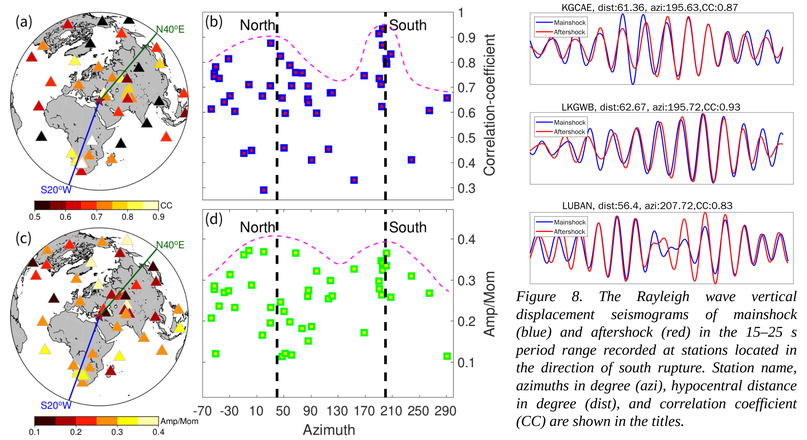

Figure 7. Far-field Rayleigh wave analysis. (a) Spatial distribution of stations. Triangles denote the stations used for analysis, color-coded by the cross-correlation coefficients (CCs) between 15 to 25 s Rayleigh waves of the mainshock waveforms and its M5.3 aftershock waveforms. The dark green line and word indicate the direction of the northeast rupture. The blue line and word indicate the direction of the southwest direction. (b) CCs distribution as a function of the station azimuth. The vertical black dashed lines indicate the northeast and southwest rupture directions. The pink dash curve indicates the envelope delineating the distribution pattern of CCs. (c) Spatial distribution of stations. Triangles denote the stations used for analysis, color-coded by [waveform amplitude ratio]/[seismic moment ratio] between the mainshock and the aftershock. (d) [Amplitude ratio]/[moment ratio] distribution as a function of the station azimuth.

Figure 8. The Rayleigh wave vertical displacement seismograms of mainshock (blue) and aftershock (red) in the 15–25 s period range recorded at stations located in the direction of south rupture. Station name, azimuths in degree (azi), hypocentral distance in degree (dist), and correlation coefficient (CC) are shown in the titles.

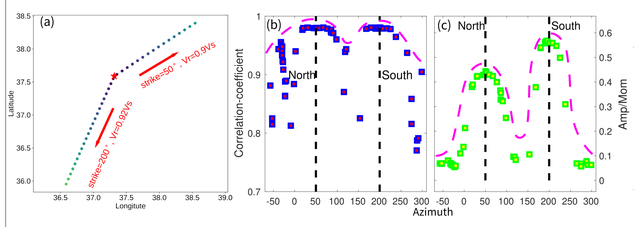

*Figure 9. Synthetic tests. (a) Input bilateral rupture propagation. The northeast speed is 0.9*Vs, and the southwest rupture is 0.92*Vs. (b) Cross-correlation Coefficients (CCs) distribution as a function of azimuth. The pink dash curve indicates the envelope delineating the distribution pattern of CCs. (c) Amplitude ratio over the seismic moment ratio.*

Earthquake Supercycle

The long-term slip rates inferred from GPS date: Pazarcık segment - 7 mm/year, Amanos segment - 3 mm/year.

The expected maximum and the actual magnitudes: 7.3 v.s. 7.49+ (Pazarcık segment); 7.4 v.s. 7.49+ (Amanos segment; Güvercin et al., 2022).

Larger than expectation; supercycle model.

We calculate the moment accumulation history: moment accumulation = moment build up – release by major (M>=7) events – release by background seismicities (M<7).

The moment build-up rate: m'=μ·L·H·r, where μ is the rock rigidity inferred from the 1D model, L is the segment length, H is the seismogenic zone depth, and r is the long-term fault slip rates.

Major earthquakes (M>=7): historical investigations (Figure 11a).

Background seismicities: Gutenberg-Richter (G-R) law.

Two scenarios: a low accumulation case with b values around 0.9, and a high accumulation case with b values around 1.1 (Güvercin et al., 2022).

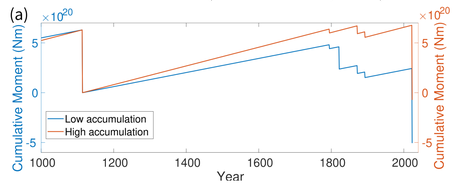

Figure 10. (a) History of potential moment accumulation on the EAF segments involved in the Mw 7.8 mainshock. The blue curve is the moment history of the low accumulation case, and the orange curve is the moment history of the high accumulation case. See text for details. The last big drop is the moment released by the 2023 Mw 7.85 event.

Low accumulation scenario: the net moment accumulation between 1114 and 2022 is approximately 32% of the coseismic moment of the 2023 Mw 7.85 mainshock.

High accumulation case: the percentage is 90%.

Implication for San Andreas-San Jacinto Fault System

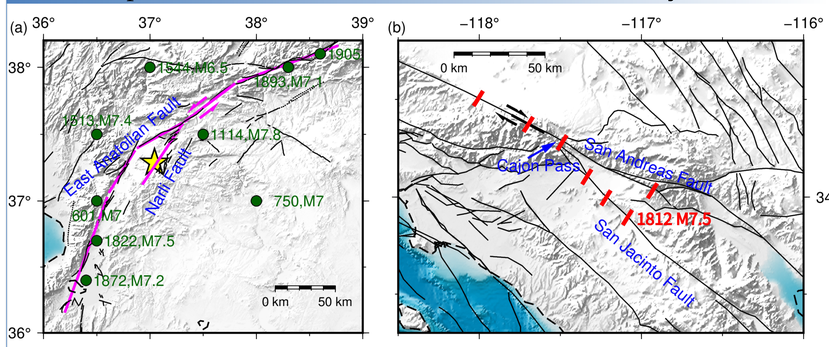

Figure 11. Map of the East Anatolian Fault and San Andreas Fault systems. The magenta arrows in (a) and black arrows in (b) show fault motions. The yellow star in (a) denotes the epicenter of the 2023 Mw7.8 event. The green dots and numbers in (a) indicate major historical earthquakes on the EAF. Red bars in (b) represent the paleoseismic sites of the early 1800 earthquake, adapted from Lozos (2016).

Table 1. Comparison between the East Anatolian Fault and the San Andreas Fault.

	East Anatolian Fault	San Andreas Fault
Fault type	Left-lateral strike-slip fault	Right-lateral strike-slip fault
Long term slip rate	<= 10 mm/yr	>= 16 mm/yr
Latest events (year, magnitude)	1872, M7.2; 1822, M7.5; 1893, M7.1.	1857, M7.9; 1812, M7.5; 1726.
Fault length	370 km	~500 km (south California part)
Supercycle duration	>=900 year	~ 1000 year

References

Ji, C., Wald, D. J. & Helmberger, D. V. Source Description of the 1999 Hector Mine, California, Earthquake, Part I: Wavelet Domain Inversion Theory and Resolution Analysis. Bull. Seism. Soc. Am. 92, 4, 1192–1207 (2002).

Meng, L., Zhang, A. & Yagi, Y. Improving back projection imaging with a novel physics-based aftershock calibration approach: a case study of the 2015 Gorkha earthquake. Geophys. Res. Lett. 43, 628–636 (2016).

Güvercin, S. E., Karabulut, H., Konca, A. Ö., Doğan, U., & Ergintav, S. Active seismotectonics of the East Anatolian Fault. Geophys. J. Int. 230, 1, 50–69 (2022).

Vallée, M., & Dunham, E. M. Observation of far-field Mach waves generated by the 2001 Kokoxili supershear earthquake. Geophys. Res. Lett. 39, L05311 (2012).

Lozos, J. C. A case for historic joint rupture of the San Andreas and San Jacinto faults. Science Advances, 2, 3, e1500621 (2016).